

PAPER • OPEN ACCESS

Diamond nanoneedles for biosensing

To cite this article: Mariam Quarshie *et al* 2025 *Nanotechnology* **36** 165501View the [article online](#) for updates and enhancements.

You may also like

- [Roadmap on printable electronic materials for next-generation sensors](#)
Vincenzo Pecunia, Luisa Petti, Joseph B Andrews et al.
- [Hybrid combination of advanced oxidation process with membrane technology for wastewater treatment: gains and problems](#)
Chhahalal Regmi, Yuwaraj K Kshetri and S Ranil Wickramasinghe
- [Green materials in semiconductors: perspective from the IRDS beyond-CMOS roadmap](#)
Akiko Ueda, Hiroyuki Akinaga, Sapan Agarwal et al.

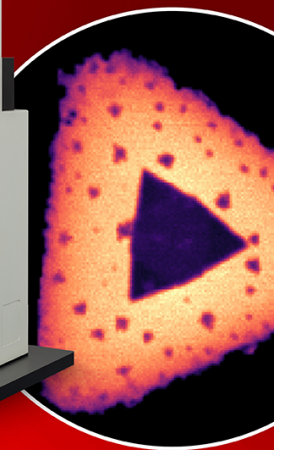
EDINBURGH
INSTRUMENTS

RMS1000 MULTIMODAL CONFOCAL MICROSCOPY

- + Raman
- + Photoluminescence
- + Second Harmonic Generation
- + Fluorescence & Phosphorescence Lifetime



SCAN ME



VISIT OUR WEBSITE FOR MORE DETAILS



edinst.com

Diamond nanoneedles for biosensing

Mariam Quarshie¹ , Lena Golubewa^{2,3} , Caterina Giraulo⁴ , Silvana Morello⁴ ,
Claudia Cirillo⁵, Maria Sarno⁵ , Bo Xu¹, Priyadharshini Balasubramanian⁶,
Yuliya Mindarava⁶, Marijonas Tutkus^{2,7,8}, Alexander Obratsov¹, Fedor Jelezko⁶,
Polina Kuzhir^{1,*}  and Sergei Malykhin¹ 

¹ Department of Physics and Mathematics, University of Eastern Finland, Joensuu, Finland

² State Research Institute Centre for Physical Sciences and Technology, Vilnius, Lithuania

³ Institute for Chemical Physics, Vilnius University, Vilnius, Lithuania

⁴ Department of Pharmacy, University of Salerno, Fisciano, SA, Italy

⁵ Department of Physics 'E.R. Caianiello', and NANO MATES Research Centre, University of Salerno, Fisciano, SA, Italy

⁶ Institute for Quantum Optics & IQST, Ulm University, Ulm, Germany

⁷ MB Platformina, Vilnius, Lithuania

⁸ Institute of Biotechnology, Life Sciences Centre, Vilnius University, Vilnius, Lithuania

E-mail: polina.kuzhir@uef.fi

Received 21 September 2024, revised 14 February 2025

Accepted for publication 21 February 2025

Published 6 March 2025



CrossMark

Abstract

Nanoparticles and nanomaterials are revolutionizing medicine by offering diverse tools for diagnosis and therapy, including devices, contrast agents, drug delivery systems, adjuvants, therapeutics, and theragnostic agents. Realizing full applied potential requires a deep understanding of the interactions of nano dimensional objects with biological cells. In this study, we investigate interaction of single-crystal diamond nanoneedles (SCDNNs) containing silicon vacancy (SiV⁻) color centers with biological substances. Four batches of the diamond needles with sizes ranging between 200 nm and 1300 nm and their water suspensions were used in these studies. The human lung fibroblast cells were used for the proof-of-concept demonstration. Employing micro-photoluminescence (PL) mapping, confocal microscopy, and lactate dehydrogenase (LDH) viability tests, we evaluated the cellular response to the SCDNNs. Intriguingly, our investigation with PL spectroscopy revealed that the cells and SCDNNs can coexist together with approved efficient registration of SiV⁻ centers presence. Notably, LDH release remained minimal in cells exposed to optimally sized SCDNNs, suggesting a small number of lysed cells, and indicating non-cytotoxicity in concentrations of 2–32 $\mu\text{g ml}^{-1}$. The evidence obtained highlights the potential of SCDNNs for extra- or/and intracellular drug delivery when the surface of the needle is modified. In addition, fluorescent defects in the SCDNNs can be used for bioimaging as well as optical and quantum sensing.

Keywords: diamond needles, SiV⁻ centers, photoluminescence, biomedical applications

* Author to whom any correspondence should be addressed.



Original content from this work may be used under the terms of the [Creative Commons Attribution 4.0 licence](https://creativecommons.org/licenses/by/4.0/). Any further distribution of this work must maintain attribution to the author(s) and the title of the work, journal citation and DOI.

1. Introduction

Nanoscience and nanotechnology have transformed our understanding of the physical world [1, 2], especially at the nanoscale and single-molecule level [3–6], where quantum mechanical effects become significant [7, 8]. Nanostructures, often consisting of multiple atoms or molecules [9], exhibit remarkable behaviors that bridge the quantum and classical regimes [10], opening new frontiers in materials science and technology [11, 12]. Among these, color centers in diamond stand out as particularly intriguing examples. The combination of high surface area, strategic placement of nitrogen-vacancies (NV) and silicon-vacancies (SiV) color centers, and the intrinsic thermal properties of diamond underscores the viability of nanosized diamonds for both optical and quantum sensing technologies.

When materials are reduced to dimensions below 100 nm [13], they undergo significant transformations in their physical and chemical properties [14, 15]. These transformations include altered electronic bandgaps, reduced melting points, and enhanced surface reactivity [16, 17]. These changes have catalyzed major advancements in fields such as quantum sensing, quantum computing, and biomedicine [18, 19].

Among the diverse range of nanostructures under investigation, carbon-based nanoparticles have attracted special attention due to unique combination of stability, ease of synthesis, and biocompatibility [20, 21]. Diamond, a carbon allotrope, has particularly emerged as a leading material [22] in nanomedicine, with the potential to revolutionize medical interventions, especially in minimally invasive procedures [23]. Due to chemical and biological inertness diamond does not induce coagulation or inflammatory responses [24] while its semiconductor nature opens up possibilities for use as an electrochemical electrode [23]. Also, there are number of strategies that can be applied to modify its surface for targeted delivery and controlled release in cells [25, 26]. While diamond is not biodegradable in the traditional sense, its inertness, ability to be safely eliminated from the body in nanodiamond form, and unique functional properties make it a valuable material for medical technologies.

Bulk diamonds can be engineered [27] into arrays of miniaturized, one-dimensional structures using techniques such as direct-write laser ablation or chemical etching. Alternatively, chemical vapor deposition (CVD) can be employed for one-dimensional diamond structures manufacturing in form of needle-like crystallites [24]. This process includes polycrystalline film deposition with needle-like diamond crystallites embedded into disordered carbon and disordered fraction removal by oxidation to create freestanding diamond needles [28]. The resulting miniaturized diamonds retain the advantageous properties of their bulk, making them suitable for a wide range of applications. For instance, high-aspect-ratio diamond arrays are well-suited for navigating complex biological environments and can target diseased cells with minimal disruption to surrounding membranes [29, 30].

The exceptional thermal conductivity of diamond facilitates efficient temperature distribution, enabling the use of color centers throughout the entire crystal volume for intracellular thermometry. By combining precise engineering of color centers with shape control, multifunctional diamond nano sensors can be realized-NV centers in the thinner half of the crystal for highly efficient magnetic field sensing, and SiV centers in the thicker half to provide a high signal-to-noise ratio for thermometry. With appropriate functionalization, these structures could serve as a powerful nanoscale platform for intracellular multifunctional diagnostics and treatment [31, 32].

Despite the promising potential of diamond nanostructures, significant safety concerns remain regarding their interactions with biological systems [21]. Rigorous research is needed to thoroughly assess their *in vivo* safety and environmental impact, particularly in biomedical applications [33]. Furthermore, challenges such as developing cost-effective and efficient methods for producing diamond nanocarriers, as well as translating laboratory discoveries into practical clinical treatments, must be addressed to fully realize the potential of these materials [23].

This study focuses on single-crystal diamond nanoneedles (SCDNNs), which are needle-shaped diamond structures [34] with at least one dimension less than 100 nm. The research aims to deepen our understanding of how SCDNNs interact with mammalian cells models, evaluate their cytotoxicity, and explore their potential applications in cellular sensing and drug delivery. By harnessing the unique fluorescence and surface chemistry properties of SCDNNs, this study seeks to make a significant contribution to the field of nanomedicine, advancing the possibilities for treating and diagnosing diseases at the cellular level.

2. Experimental procedure

2.1. Synthesis and characterization of SCDNNs

The fabrication process for the SCDNNs consists of combination of CVD and selective oxidation techniques. These are outlined in [28, 35]. We analyzed SCDNNs of three different sizes as well as SCDNNs with modified surfaces. To obtain the SCDNNs of different sizes we varied duration of synthesis maintaining methane concentration in methane–hydrogen gas mixture of 3% and substrate temperature of around 900 °C. Samples 1, 2 and 3 were synthesized in CVD processes with duration of 1 h, 50 min and 30 min, respectively. To fully oxidize disordered carbon matrix from the synthesized films and isolate SCDNNs we placed the samples into the oven for 20 h at 630 °C in air atmosphere. To obtain sample 4 we synthesized similar SCDNNs as in sample 1 but applied also heating up to 1100 °C in vacuum (2×10^{-1} mbar) for 30 min after selective oxidation step resulting in the transformation of surface layers of SCDNNs to sp^2 carbon as described in [36]. This additional

treatment was produced for the needles located on the same Si substrate. The sp^2 surface allows to extend functionalization potential of SCDNNs important for biological applications. Thus, utilizing sample 4 we preliminary analyze here cytotoxicity of the core-shell SCDNNs. All SCDNNs were synthesized on silicon substrates (p-type boron-doped, size of $30 \times 30 \text{ mm}^2$) to form SiV^- color centers in them [37].

The morphology of the obtained SCDNNs situated on Si chips which were used as substrates for CVD growth were examined using a ZEISS LEO GEMINI 1550 and TESCAN VEGA COMPACT scanning electron microscopes (SEMs) with an electron beam acceleration voltage of 10 and 30 kV, respectively. Optical characterization was performed using the RENISHAW inVia Raman spectrometer. The spectrometer operated in both Raman and photoluminescence (PL) modes with excitation wavelength of 514.5 nm and air objective of $\times 20$ magnification.

For the experiment on cell-SCDNN interaction, a suspension of SCDNNs in Dulbecco's phosphate buffered saline (DPBS) was prepared. The as synthesized SCDNNs on silicon substrates were rinsed with $500 \mu\text{l}$ of PBS and collected in separate tubes. The resulting concentrations of SCDNNs in suspensions were estimated based on SEM images as described below (see 3.1 and 3.2). Freshly prepared suspensions were then immediately added to the cells in a volume ratio 1:4 (SCDNNs: cells) to avoid significant dilution of cell culture medium with PBS and a reduction of nutrients concentration.

2.2. Biological samples and experiments

As model mammalian cells we chose human fibroblast cells (MRC-5). They were cultured in minimal essential medium (MEM) supplemented with 1% (v/v) L-glutamine, 1% (v/v) Penicillin/Streptomycin, 1% (v/v) sodium pyruvate, and 10% (v/v) heat-inactivated fetal bovine serum (FBS) under controlled conditions of 5% CO_2 at 37°C .

Cells (20 000 cells/well) were seeded in 24-well plates on sterilized round glass coverslips and maintained for 24 h in a controlled environment of 5% CO_2 at 37°C to facilitate cell attachment to the plate surface. Then cells were rinsed with DPBS, and $400 \mu\text{l}$ volume of fresh medium was added to the cells plus $100 \mu\text{l}$ volume of SCDNNs suspension (resulting in a final volume of $500 \mu\text{l}$ per well).

In this experiment, we used the colorimetric kit assay (Cytotoxicity Detection Kit PLUS (#04-744-926-001; Roche) to measure lactate dehydrogenase (LDH) release in cell culture supernatant and in this way evaluate cytotoxicity of our fabricated SCDNNs samples.

Control wells were administered with $100 \mu\text{l}$ of DPBS. The concentration of SCDNNs in the suspension used was estimated in the following section using SEM images. These estimations were crucial for conducting experiments with varying concentrations of SCDNNs to determine the critical concentration that affects cell viability.

After 48 h of treatment period, the cell culture medium (cells supernatants) was collected to measure the LDH release,

a marker of cell cytotoxicity, as reported below, while the cells were fixed with 4% (v/v) paraformaldehyde in $1 \times$ DPBS for 10 min, permeabilized with 0.2% (v/v) Triton X-100 in $1 \times$ DPBS for 5 min and washed twice with DPBS to remove weakly-bound materials from cell surface. The cells nuclei were stained with DAPI (1:3000; Sigma-Aldrich). Coverslips were mounted onto slides, securing the cells in the mounting medium between the slide and coverslip. The prepared cells were used to perform optical investigation as specified below.

The cytotoxicity assessment was performed following a 48-hour incubation period of cells with SCDNNs. Wells containing untreated cells acted as the negative control, monitoring the basal release of LDH, while wells treated with lysis solution to induce maximum LDH release served as the positive control. The lysis solution from the cytotoxicity detection kit PLUS (#04-744-926-001; Roche) was added to the positive control wells and allowed to incubate for 15 min.

Subsequently, $100 \mu\text{l}$ of medium was collected from each well, including those containing positive and negative controls, as well as treated cells. This medium was combined with the reaction mix from the cytotoxicity detection kit PLUS ($100 \mu\text{l}$) and allowed to incubate for 10 min at room temperature, shielded from light. Following incubation, $50 \mu\text{l}$ of stop solution was added to each well, and the absorbance of the samples was assessed at 490 nm using a spectrophotometer (Thermo Scientific Multiskan® Spectrum). According to the manufacturer's instructions, calculating the percentage of cytotoxicity requires the use of three controls: the background control, which determines the LDH activity present in the assay medium used for culturing the cells; the negative control, which measures the LDH activity released from untreated cells; and the positive control, which represents the maximum releasable LDH activity from the cells. All measurements were performed in triplicate to ensure a robust estimation of cytotoxicity. The percentage of cytotoxicity was calculated by subtracting the absorbance of the negative control from the absorbance values of the samples, as follows:

$$\text{Cytotoxicity (\%)} = \frac{\text{Abs}_{\text{exp}} - \text{Abs}_{\text{neg.control}}}{\text{Abs}_{\text{pos.control}} - \text{Abs}_{\text{neg.control}}} \times 100. \quad (1)$$

While LDH release indicates membrane disruption, the absence of significant LDH release does not necessarily imply that nanoneedles have no impact on cellular activity. Sublethal effects, such as changes in metabolic activity, gene expression, or intracellular signaling, may still occur without causing cell lysis. Investigating the full range of interactions between nanoneedles and cells is a complex but essential task. To gain a comprehensive understanding of these effects, complementary assays—such as metabolic activity assays (e.g. MTT or resazurin), oxidative stress markers, or gene expression profiling—can be employed to evaluate how nanoneedles influence cellular function, which is out of the scope of present paper.

2.3. Optical investigation of biological samples

To perform optical investigation of the prepared cells we used the RENISHAW inVia Raman spectrometer, confocal optical microscope ZEISS LSM-800 and home-built confocal optical setup equipped with spectrometer.

Utilizing inVia Raman spectrometer we conducted micro-PL mapping, aiming to determine the spatial location of SCDNNs in sample 3 within the cell medium mounted between slide and coverslip. This mapping was achieved by detecting the PL from SiV⁻ and NV centers in the SCDNNs. The procedure involved capturing the PL intensity while moving a stage with a fixed sample on it to scan the laser beam throughout a specified area of the sample. We used scanning steps of 0.5 and 2 μm for this procedure. Using the gathered array of spectral data, we plotted a 2D map indicating the positions of PL sources fluorescent at different wavelengths.

In the ZEISS confocal microscope, we used three detection channels: blue, green, and red. For the blue channel, we applied a combination of laser excitation of 405 nm and emission detection in the range 420–600 nm usually used for DAPI fluorescent stain. In the green channel, the excitation laser was 488 nm detecting in range of 500–650 nm. The red channel was used to register PL signal from SCDNNs. The main source of PL in SCDNNs is SiV⁻ color centers with zero-phonon line (ZPL) at 738 nm containing approximately $\sim 70\%$ of total PL of SiV⁻ centers [38]. However, the detector in the used ZEISS system registers light with wavelength only up to 700 nm, capturing only the small left tail of the PL line. Thus, to be able to register the PL, we used excitation with two lasers having 488 and 561 nm wavelengths detecting the light in the range of 656–700 nm. The oil objective had magnification of $\times 63$ and numerical aperture (NA) of 1.4.

The home-built confocal setup had excitation laser with wavelength of 532 nm, oil objective with magnification of $\times 100$ and NA of 1.35, EXCELITAS avalanche photodiode as a detector and PRINCETON INSTRUMENTS SpectraPRO HRS-300 spectrometer. For the PL mapping we applied a combination of long pass of 560 nm and short pass of 800 nm to visualize cell, and bandpass filter of 740/13 nm to visualize SiV⁻ centers.

3. Results and discussion

3.1. Characterization of SCDNNs

Characteristic SEM images of as-prepared SCDNNs are shown in figure 1. The Si substrates on the images look rough because of modifications during CVD and oxidation processing. Based on these images, we calculated the average length of the SCDNNs in each sample to be $1.4 \pm 0.2 \mu\text{m}$ for samples 1 and 4 (figures 1(a) and (d)), $1.15 \pm 0.15 \mu\text{m}$ for sample 2 (figure 1(b)), and $320 \pm 110 \text{ nm}$ for sample 3 (figure 1(c)). These measurements indicate a variability in nanoneedle length, which could affect their interaction with cells. Additionally, the weight of SCDNNs in each sample

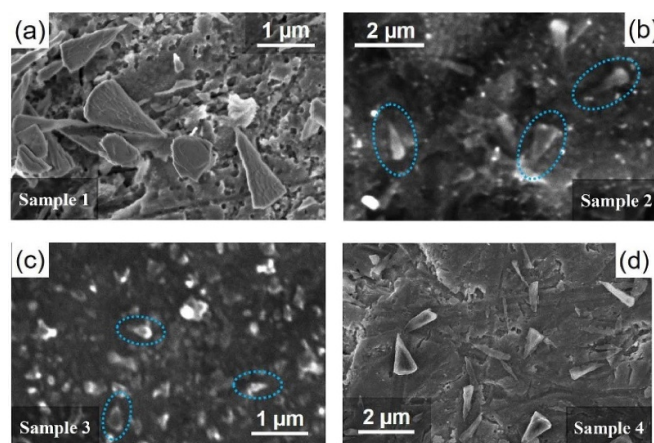


Figure 1. Scanning electron micrographs (SEMs) of SCDNNs for samples 1 (a), 2 (b), 3 (c), and 4 (d). The images illustrate the morphology, characteristic sizes, and distribution of SCDNNs on the silicon plates. Turquoise blue highlights the individual SCDNNs.

was estimated by calculating the volume based on the average observed dimensions and assuming a conical shape, in combination with the density of bulk diamond. The estimated weights were 100 μg , 24 μg , 28 μg , and 80 μg for samples 1 through 4, respectively. These weight estimations were crucial for determining the concentration of SCDNNs used for each sample (table 1), as there is a threshold value of concentration after which cytotoxicity is triggered.

Raman spectroscopy confirmed the crystalline quality of the SCDNNs across all samples, with a consistent diamond peak observed at approximately 1330 cm^{-1} (figures 2(a) and (b)) [38]. The highest intensity was recorded for sample 1, while the lowest intensity was observed for sample 3 (figure 2(a)). This variation in intensity can be attributed to differences in the size of the diamond nanoneedles. The larger needle contains more substance producing larger Raman intensity. Notably, sample 4 exhibited additional D and G bands at 1360 cm^{-1} and 1590 cm^{-1} . The D band can be attributed to the presence of defects or disorder in sp^2 -bonded carbon, possibly from graphitic impurities or surface defects whilst the G band reflects the crystalline structure of the sp^2 carbon [39, 40]. The observed peaks for sp^2 carbon confirm successful graphitization of surface layers of SCDNNs in sample 4 [39].

PL studies further characterized the SCDNNs, revealing strong emissions from SiV⁻ color centers in all samples, with a ZPL at 738 nm (figure 2(d)). Samples 1 and 2 also exhibited PL signals from neutral nitrogen-vacancy (NV⁰) centers, with a ZPL at 575 nm (figure 2(c)). The absence of detectable NV⁰ signals in sample 4 suggests efficient absorption of the weak NV⁰ PL signal by the surrounding shell structure.

The variations in PL intensity across samples 1–4 are attributed to differences in the sizes of the SCDNNs and the presence of sp^2 carbon [34]. For instance, sample 4, a graphitized version of sample 1, showed the lowest PL intensity due to the presence of sp^2 carbon. These findings, highlighting

Table 1. Comparison of calculated cytotoxicity levels between samples and controls.

	Control [-]	Control [+]	Sample 1	Sample 2	Sample 3	Sample 4
Cytotoxicity [%]	0	100.00	0.74	0.44	-6.67	-4.00
Optical density [OD 490 nm]	0.051	0.163	0.051	0.051	0.043	0.046
Weight of SCDNNs [μg]	—	—	20–80	5–19	6–22	16–64
SCDNNs concentration [$\mu\text{g ml}^{-1}$]	—	—	8–32	2–8	2–9	6–26
SCDNN length [nm]	—	—	1300–1500	1000–1300	200–420	1300–1500

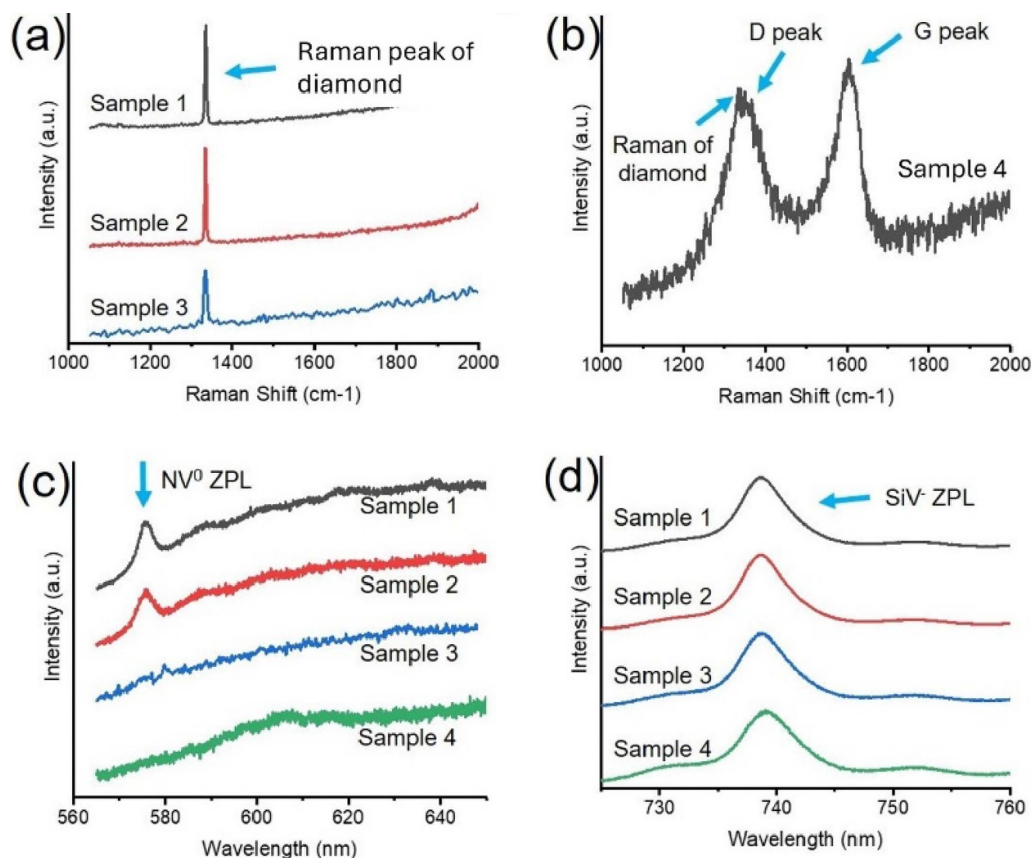


Figure 2. Typical Raman (a, b) spectra of samples 1–3 (a) and 4 (b), and PL spectra (c), (d) of obtained SCDNNs. Turquoise blue arrows indicate characteristic peaks representing the main materials in the samples (a), (b), as well as the zero-phonon lines (ZPLs) of NV^0 (c) and SiV^- color centers (d). Graphs (c) and (d) demonstrate PL of the samples in different spectral range for clarity.

the presence of both SiV^- and NV^0 centers, are crucial for the potential application of SCDNNs in quantum sensing and bioimaging.

3.2. Cytotoxicity test

The results of the cytotoxicity tests are summarized in table 1. The concentration of SCDNNs in the test environment (consisting of cells and SCDNNs) was estimated based on the previously measured weights of SCDNNs (see table 1) in each sample. We assumed that 20%–80% of the SCDNNs were transferred from the silicon substrate to the cell culture medium during the tests.

Considering the limited number of replicates in the LDH assay, the statistical dispersion of the data, and the

experimental setup, techniques, and protocols employed, we estimate the upper limit of the total error in the reported cytotoxicity values to be 10%. Therefore, the negative cytotoxicity values in table 1 are within the error margin.

Optical density (OD) measurements, obtained at 490 nm using the Thermo Scientific Multiskan® Spectrum spectrophotometer, were used to assess formazan production, a direct indicator of cell viability. Lower formazan production correlates with decreased light absorption, reflecting healthier cells, while increased production suggests reduced cell viability. Our results showed very low OD values, indicating minimal formazan production across the samples. These low OD readings correspond to minimal LDH activity, a marker of reduced cell membrane damage, and thus suggest limited NADH production.

The cytotoxicity percentages, calculated using equation (1) (see table 1), were significantly lower than the positive control (100%), indicating a minimal number of lysed cells. This supports the conclusion that the SCDNNs concentrations and duration of incubation used in this study are non-toxic to the cells tested, demonstrating their potential safety for further biological applications.

3.3. Penetration of SCDNNs into the cells

Figure 3 presents a detailed microscale optical analysis of an individual biological cell exposed to sample 3, with a focus on the PL emitted by SiV⁻ containing SCDNNs and their spatial distribution within or on the cellular surfaces. Sample 3 was selected for this study due to its small nanoneedle size, which shows great potential for efficient cellular penetration. Data were acquired at two spatial resolutions: a broad spectral overview using a 2 μm spatial scan step (figure 3(b)) and a higher-resolution examination employing a 0.5 μm spatial scan step (figure 3(c)).

The spectra and PL map presented in figures 3(a) and (b) were generated from data obtained within the 520 to 800 nm spectral range. This range is crucial for capturing key features associated with SiV⁻ centers and the cell. Analyzing obtained data, we found that the highest contrast of the cell is observed in the narrower 585 to 610 nm spectral range, as shown in the inset of figure 3(a). This specific range was employed to create PL map in figure 3(b). To obtain the high-resolution PL map (figure 3(c)) we used the same narrow spectral range together with the spectral range covering PL of SiV⁻ center (from 725 to 750 nm). The image in figure 3(c) combines both high-resolution PL maps where the signal of the second map is presented in purple and located only in one region of the map marked with black circle. The resulting image provides a more precise visualization of the cell and the SiV⁻ centers within the cell.

In these PL maps, the brightness of each pixel corresponds to the integrated area under the PL emission curve within the specified spectral ranges. Figure 3(a) highlights a rectangular region of interest that distinguishes the cell from the surrounding background and effectively isolates the PL signal from the SiV⁻ centers within the SCDNNs inside the cell. The high-resolution map in figure 3(c) reveals varying PL intensities, represented by colors ranging from deep blue to yellow. Bluish regions typically indicate lower PL intensity around the cell's periphery, while light blue regions within the cell show moderate intensity. The most intense PL signals, marked in yellow, were found in specific cellular areas.

Further analysis of these bright yellow regions revealed in one of them PL signal characteristic of SiV⁻ centers, with a ZPL centered at 738 nm. These signals are overlaid in purple in figure 3(c), as reflected in the blue spectrum (figure 3(d)), confirming the emission from SiV⁻ centers. In contrast, the orange spectrum, representing a random area within the cell, showed no SiV⁻ signal (figure 3(d)).

The data presented suggest that the SCDNNs are either positioned on the surface of the investigated cells or have been internalized. The presence of strong PL signals specifically from SiV⁻ centers within the intracellular regions indicates that some of these nanoneedles may have been actively taken up by the cell, potentially into a food vacuole, as suggested by the pink overlay observed in figure 3(c). This observation aligns with the potential mechanism of cellular uptake, such as endocytosis, where the cell internalizes external particles.

To further confirm whether the SCDNNs were internalized by the cell or merely positioned on its surface, we employed confocal mapping techniques. The optical microscopy images (figures 4(a) and (b)) provided a general view of the morphology of the same cell analyzed in figure 3. Figure 4(b) offers an enlarged perspective for greater detail. The confocal microscopy images (figures 4(c)–(f)), in turn, offer more definitive insights. The green channel (figure 4(c)) clearly outlines the fibroblast cells, while the blue channel (figure 4(d)) shows the DAPI-stained nuclei of the cells, confirming their structural integrity. When these channels are overlaid in figure 4(e), the spatial relationship between the cell and its nucleus becomes apparent. The key observation comes from figure 4(f), where an enlarged image of the same cell analyzed in figure 3 is shown. In this image, the white inset highlights the spatial region used in further investigations (see figure 5) and combining region containing SiV⁻ PL (see figure 3) and cell nucleus.

To verify the internalization of SCDNNs, a z-stack scan was performed using the same confocal microscope (ZEISS). The z-stack images are presented in figure 5 offering insights into the spatial positioning of SCDNNs within fibroblast cells. To initiate this analysis, we first estimated the amount of space occupied by the selected cell. The estimated cell's volume was then scanned with a step size of 680 nm, examining the localization of SCDNNs across different focal planes. The scanned results were detected with three filters/channels (green, blue, and red channel).

The blue channel (405 nm excitation) provided a focused image of the cell nucleus at a focal plane of 3.06 μm , confirming imaging of a central section of the cell. Other focal planes viewed through this channel are much blurry than the one at 3.06 μm focal plane. The red channel, designed to detect the PL signal from the SiV⁻, revealed the presence of these SiV⁻ centers only at Z position of 3.74 μm (white outline insert). The appearance of SCDNNs exclusively at this Z-position strongly suggests active uptake by the fibroblast cells, possibly through phagocytosis. This internalization is significant as it highlights the potential utility of SCDNNs in intracellular drug delivery systems, where they can be employed to transport therapeutic agents directly into cells.

The custom-built confocal microscope was employed to address the limitations of the commercial setup in detecting PL signals at 738 nm.

We analyzed spectra from different parts of the selected sample of cells to verify similar behavior all over the sample. Specifically, we looked at regions containing bright spots

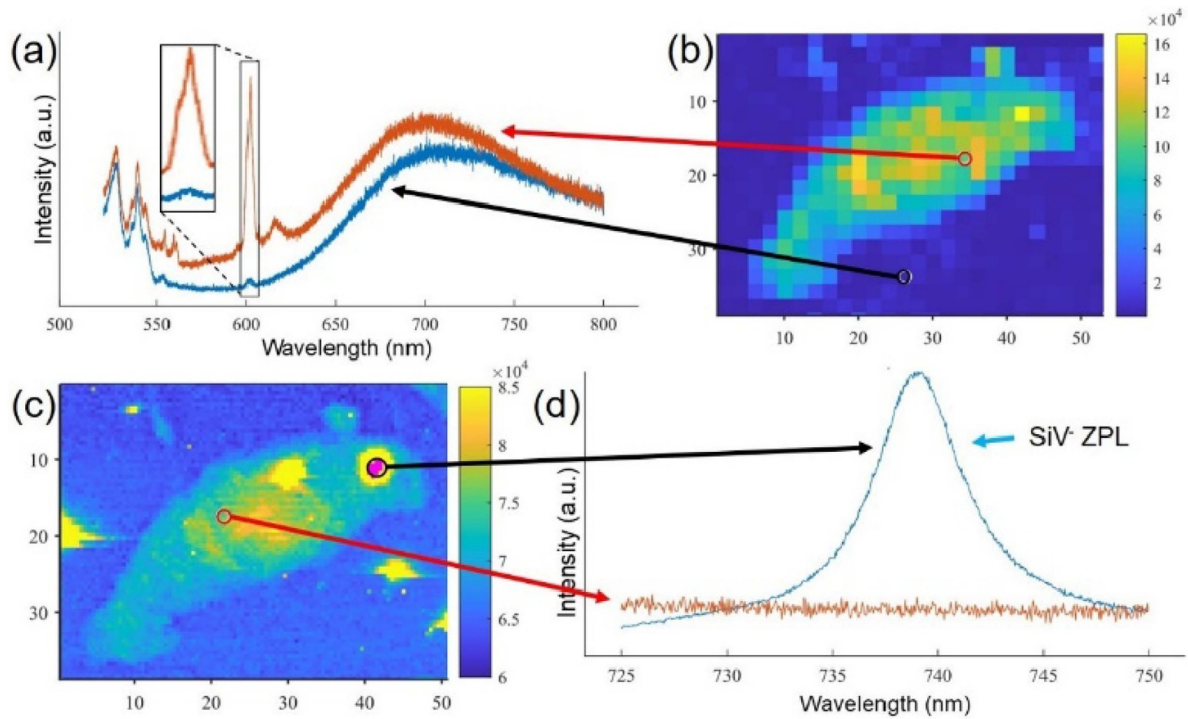


Figure 3. Photoluminescence (PL) spectra (a), (d), and map (b), (c) were obtained with RENISHAW InVia Raman spectrometer. The PL spectra and map in (a), and (b) were collected in the spectral range of 500 nm to 800 nm. Both PL map and spectra (c) and (d) were collected in the spectral range between 585 nm and 610 nm marked in (a) in insertion. The maps (b) and (c) differ in spatial resolution. 3d shows characteristic spectrum in a random place of the cell (in orange) and spot where we found signal from SiV⁻ centers (in blue).

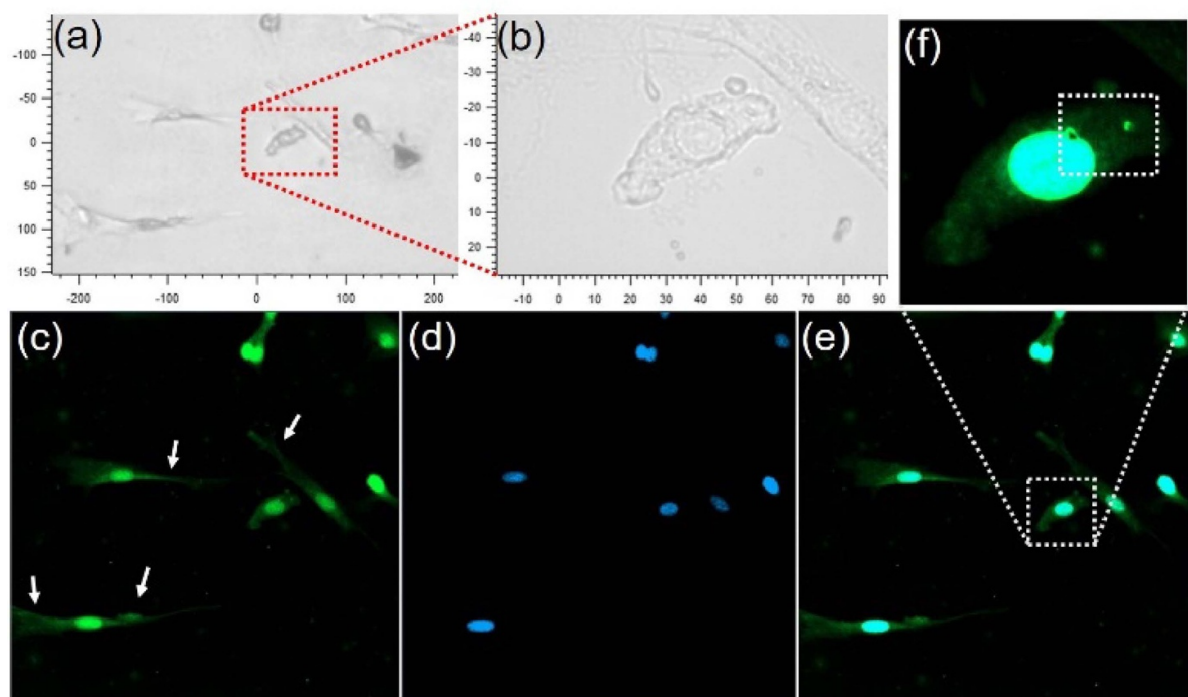


Figure 4. Images of fibroblast cells captured using optical (a), (b) and confocal microscopy (c)–(f). (a) Optical microscope image and (b) enlarged view of (a) with scale bars. LSM confocal microscope images: (c) isolated fibroblast cells in the AF 488-T2 channel (green), (d) cell nuclei stained with DAPI-T3 (blue), (e) overlay of (c) and (d), and (f) an enlarged image of the selected cell used for subsequent analysis. Panels (a), (b), and (f) show the same cell analyzed in figure 3. The white inset in (f) highlights the region containing SCDNNs and part of the cell, which is further analyzed in figure 5. The white arrows in (c) point to some bodies and legs of the cells.

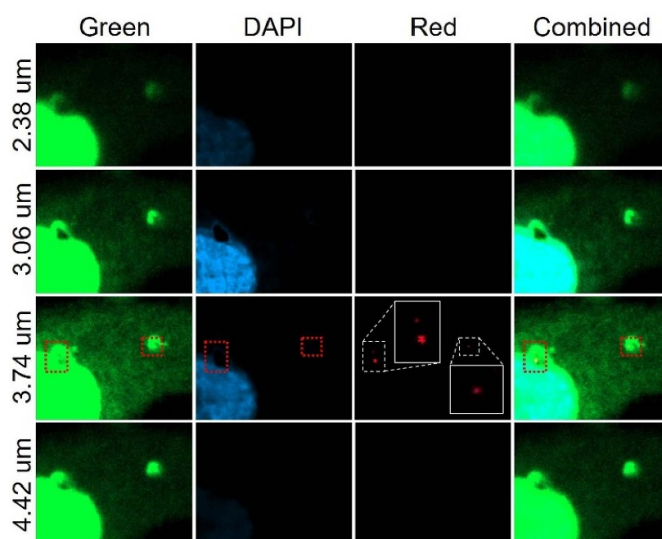


Figure 5. Optical sections at different focal planes using the LSM confocal microscope, with areas of interest highlighted in red and white inserts. Cells registered in the channel optimal for AF 488-T2 dye are shown in green (first column on the left), cell nucleus stained with DAPI-T3 is shown in blue (second column from the left), SCDNNs registered in the channel optimal for AF 750-T1 are shown in red (third column from the left), and an overlay of green, blue, and red channels is shown in the last column on the right. Illumination was provided by a 405 nm diode laser for DAPI channel, 488 nm—for Green channel and combination of 488 nm and 561 nm for Red channel. Tunable detection wavelengths for all fluorescence in the range from 400 to 700 nm optimal for each dye type (DAPI, AF 488, AF 750) using PMTs was performed.

(figure 6(c)) and compare them with darker areas (figure 6(d)) within the cell. We then carefully verified the cell's position, and concurrently observed bright spots in the SiV^- center filter map (figure 6(b)) and a broader luminescence signal in the overall map (figure 6(a)). Our findings, as depicted in figure 6, reveal a compelling correlation between bright spots observed in both broad-spectrum and narrow-band PL maps, strongly suggesting the intracellular location and distribution of the SCDNNs.

By performing a Z-scan (a) technique where the focus is moved along the optical axis in the area indicated by the white dashed line in figure 6(a), we also determined that the bright spots are located within the three-dimensional volume of the cell (figure 6(e)).

Essentially, the Z-scan helped to establish that the bright spots were not just surface features but were indeed located inside the cell. The spectral analysis identified the nature of these bright spots and the specific color centers present within the SCDNNs. The SCDNNs contain SiV^- , NV^0 , and NV^- color centers. This spectral findings were consistent with previous studies [36, 39] that have established the optical properties of these color centers in bulk diamond.

Additionally, we observed that the SCDNNs in the cell probably exist within the cell in two possible forms: as

individuals, separate particles (visible as isolated bright spots in figure 6(a)) or as clusters or groups (visible as larger, aggregated bright spots in figures 6(b) and (e)). This observation underscores the potential of SCDNNs for diverse applications. The ability to detect fluorescence emitted by these color centers within SCDNNs even when located inside a cell reinforces their promise for use in optical and quantum sensing technologies, as well as tools for investigating intracellular processes.

4. Conclusion

The synthesis of SCDNNs was optimized to achieve nano-scale sizes while incorporating SiV^- and neutral nitrogen NV^0 color centers. The research focused on their physical properties, cytotoxicity, and interactions with model mammalian cells. The main findings are summarized below:

The SCDNNs exhibited well-defined structural properties, with average lengths ranging from 320 nm to 1.4 μm across different samples. Raman spectroscopy confirmed the crystalline nature of the SCDNNs, with distinct peaks corresponding to diamond crystals, SiV^- , and NV^0 centers. Additionally, PL analysis revealed strong signals from SiV^- centers across all samples, confirming their successful incorporation into the nanoneedles. In contrast, while SCDNNs from samples 1 (1300–1500 nm), 2 (1000–1300 nm), and 3 (200–420 nm) exhibited detectable NV^0 signals, sample 4, with a similar size range to sample 1, lacked these features due to graphitization.

Performed LDH activity-based cytotoxicity tests demonstrated that the SCDNNs were non-toxic to the tested cells at specific concentrations (8–32 $\mu\text{g ml}^{-1}$, 2–8 $\mu\text{g ml}^{-1}$, 2–9 $\mu\text{g ml}^{-1}$, 6–26 $\mu\text{g ml}^{-1}$) and given durations of incubation supporting the conclusion that SCDNNs did not induce significant cytotoxic effects. These findings establish the biocompatibility of SCDNNs, making them suitable for potential biomedical applications.

Detailed PL mapping and confocal microscopy revealed that some SCDNNs were internalized into the cells. The presence of SiV^- centers within specific intracellular regions, as detected by PL signals, strongly suggested active cellular uptake, likely through mechanisms such as endocytosis or phagocytosis. This was further confirmed through z-stack scanning, which localized the SCDNNs within the three-dimensional volume of the cell.

The successful internalization of SCDNNs into cells, combined with their non-toxic nature, underscores their potential as vehicles for intracellular drug delivery or as tools for investigating cellular processes. Additionally, the ability to detect fluorescence from color centers within SCDNNs when they are inside cells highlights their promise for use in optical and quantum sensing technologies.

In summary, the study not only validates the physical and chemical properties of SCDNNs but also demonstrates their safety to mammalian cells. The findings open new avenues

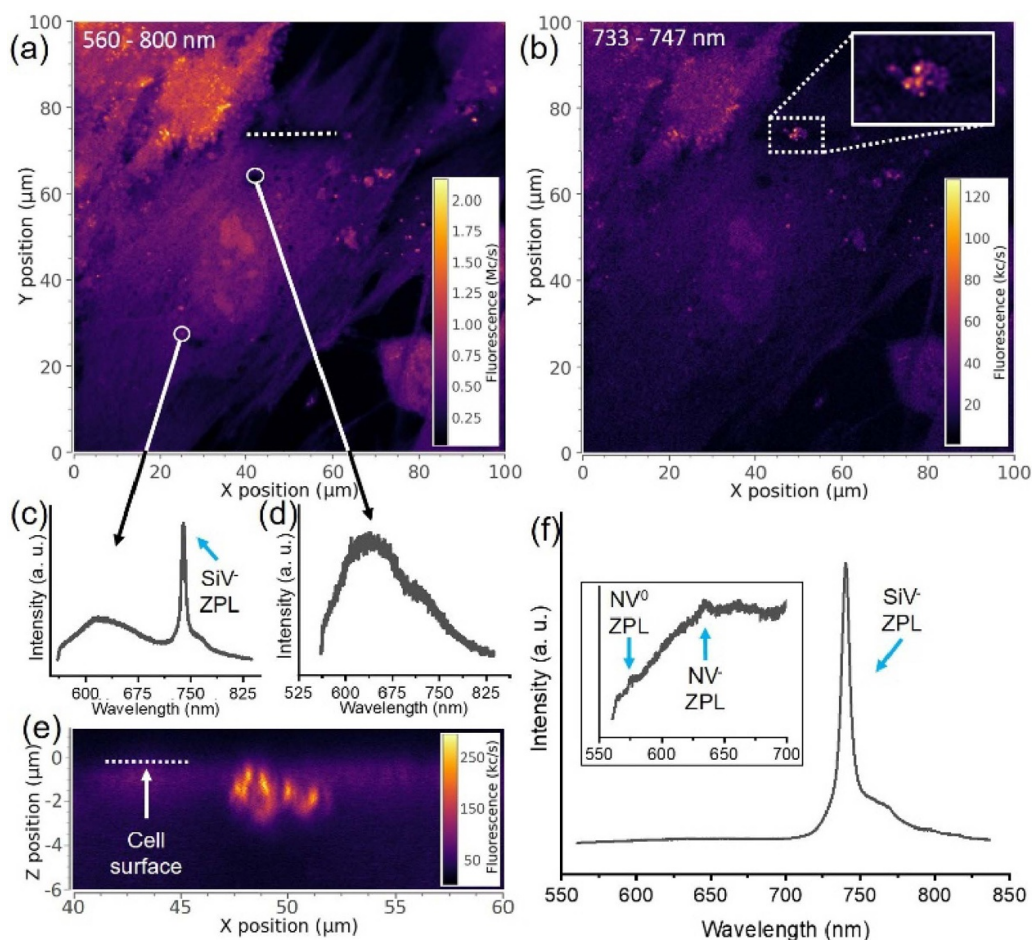


Figure 6. XY (a), (b) and Z (e) PL maps of a representative fixed cell and PL spectra (c), (d), (f) of selected areas in (a) and (b), obtained with a homebuilt confocal fluorescence microscope. (e) Shows the PL map of areas near the dotted white line in (a). The excitation light was green (532 nm), with collected luminescence light ranging from 560 to 800 nm in (a) and 733–747 nm in (b). The white rectangle insert highlights the agglomeration of identified SCDNNs.

for utilizing SCDNNs in advanced biomedical applications, including targeted drug delivery, intracellular sensing, and real-time monitoring of cellular processes.

Data availability statement

All data that support the findings of this study are included within the article (and any supplementary files).

Acknowledgment

This work was supported by the Academy of Finland (Flagship Programme PREIN, decision 368653; QuantERA project EXTRASENS, decision 361115), the Research Council of Finland (CHARACTER project, decision 357033), the Research Council of Lithuania (Nr. S-QUANTERA-24-1; S-MIP-24-58 for M. T.; S-LL-24-11 for L. G.), the Horizon Europe MSCA FLORIN Project 101086142, as well as the REC HyperQ Synergy grant.

The authors declare no conflict of interest related to this work

ORCID iDs

Mariam Quarshie <https://orcid.org/0000-0003-4290-8060>
 Lena Golubewa <https://orcid.org/0000-0003-2125-6366>
 Caterina Giraulo <https://orcid.org/0009-0008-5419-2489>
 Silvana Morello <https://orcid.org/0000-0002-6541-0997>
 Maria Sarno <https://orcid.org/0000-0001-5663-3040>
 Polina Kuzhir <https://orcid.org/0000-0003-3689-0837>
 Sergei Malykhin <https://orcid.org/0000-0001-7677-0739>

References

- [1] Adams F and Barbante C 2013 *Spectrochim. Acta B* **86** 3–13
- [2] Mansoori G 2017 An introduction to nanoscience and nanotechnology *Nanoscience and Plant–Soil Systems* vol 48 (Springer) pp 3–20
- [3] Ivanovaitė S, Paksaitė J, Kopūstas A, Karzaitė G, Rutkauskas D, Silanskas A, Sasnauskas G, Zaremba M, Jones J S and Tutkus M 2023 *J. Phys. Chem. B* **29** 6470–8
- [4] Alsamsam M, Kopūstas A, Jurevičiūtė M and Tutkus M 2022 *HardwareX* **12** e00368
- [5] Tutkus M, Chmeliov J, Trinkunas G, Akhtar P, Lambrev P and Valkunas L 2021 *J. Photochem. Photobiol. B* **218** 112174

- [6] Kopūstas A, Ivanovaitė S, Rakickas T, Pocevičiūtė E, Paksaitė J, Karvelis T, Zaremba M, Manakova E and Tutkus M 2021 *Langmuir* **11** 3428–37
- [7] Laucht A et al 2021 *Nanotechnology* **32** 162003
- [8] Platnich C, Rizzuto F, Cosa G and Sleiman H 2020 *Chem. Soc. Rev.* **13** 4220–33
- [9] Barth J, Costantini G and Kern K 2005 *Nature* **7059** 671–9
- [10] Lee J, Jeon D and Yeo J 2021 *Adv. Mater.* **47** 2006606
- [11] Thedford R, Yu F, Tait W, Shastri K, Monticone F and Wiesner U 2023 *Adv. Mater.* **5** 2203908
- [12] Stockman M et al 2018 *J. Opt.* **4** 043001
- [13] Baig N, Kammakakam I and Falath W 2021 *Mater. Adv.* **6** 1821–71
- [14] Wilde G 2021 *Adv. Eng. Mater.* **23** 2001387
- [15] Haider A, Ikram M and Rafiq A 2023 Fabrication of nanomaterials *Green Nanomaterials as Potential Antimicrobials* (Springer) pp 25–46
- [16] Gebhard F 1997 Metal—insulator transitions *The Mott Metal-Insulator Transition* vol 137 (Springer) pp 1–48
- [17] Pandey P 2022 *Recent Pat. Nanotechnol.* **1** 45–66
- [18] Zekić E, Vuković Ž and Halkijević I 2018 *Građevinar* **04** 315–23
- [19] Talebian S, Rodrigues T, Das Neves J, Sarmento B, Langer R and Conde J 2021 *ACS Nano* **10** 15940–52
- [20] Kargozar S and Mozafari M 2018 *Mater. Today* **7** 15492–500
- [21] Singh J, Nayak P, Singh G, Khandai M, Sarangi R and Kar M 2023 *Carbon* **1** 3
- [22] Zhu Y, Li J, Li W, Zhang Y, Yang X, Chen N, Sun Y, Zhao Y, Fan C and Huang Q 2012 *Theranostics* **2** 302–12
- [23] Nistor P and May P 2017 *J. R. Soc. Interface* **134** 20170382
- [24] Golubewa L et al 2020 *Sensors* **18** 5028
- [25] Tutkus M, Lundgaard C, Veshaguri S, Tønnesen A, Hatzakis N, Rasmussen S and Stamou D 2024 *J. Phys. Chem. B* **9** 2124–33
- [26] Damalas A, Vonkova I, Tutkus M and Stamou D 2022 *Sci. Rep.* **1** 13486
- [27] Quarshie M, Malykhin S, Obraztsov A and Kuzhir P 2024 *Nanotechnology* **15** 155301
- [28] Alekseev A, Tuyakova F, Obraztsova E, Korosstylev V, Klinov D, Prusakov K, Malykhin A, Ismagilov R and Obraztsov N 2016 *Phys. Solid State* **58** 2307–11
- [29] Kathuria H, Kochhar J and Kang L 2018 *Ther. Deliv.* **7** 489–92
- [30] Chiappini C, Chen Y, Aslanoglou S, Mariano A, Mollo V, Mu H, De Rosa E, He Tasciotti G, Xie E and Santoro F 2021 *Nat. Protocols* **10** 4539–63
- [31] Tian Y, Nusantara C, Hamoh T, Mzyk A, Tian X, Perona Martinez F, Li R, Permentier P and Schirhagl R 2022 *ACS Appl. Mater. Interfaces* **34** 39265–73
- [32] Uthappa T, Arvind R, Sriram G, Losic D, Kigga M and Kurkuri D 2020 *J. Drug Deliv. Sci. Technol.* **60** 101993
- [33] Nymark P et al 2020 *Small* **6** 1904749
- [34] Dementjev A, Karpicz R, Xu B, Malykhin S, Svirko Y and Kuzhir P 2024 *Appl. Phys. Lett.* **124** 211903
- [35] Malykhin S, Mindarava Y, Ismagilov R, Orekhov A, Jelezko F and Obraztsov A 2019 *Phys. Status Solidi b* **9** 1800721
- [36] Quarshie M, Malykhin S and Kuzhir P 2024 *Opt. Mater. Express* **4** 965–71
- [37] Malykhin S, Mindarava Y, Ismagilov R, Jelezko F and Obraztsov A 2022 *Diam. Relat. Mater.* **125** 109007
- [38] Khan A, Allemailem K, Alhumaydhi F, Gowder S and Rahmani A 2020 *Endocr. Metab. Immune Disord. Drug. Targets* **6** 855–68
- [39] Dychalska A, Popielarski P, Franków W, Fabisiak K, Paprocki K and Szybowicz M 2015 *Mater. Sci. Pol.* **4** 799–805
- [40] Nikhar T, Rechenberg R, Becker M and Baryshev S 2020 *J. Appl. Phys.* **23** 235305